

Mapping Polymer Molecular Order in the SEM with Secondary Electron Hyperspectral Imaging

Robert C. Masters, Nicola Stehling, Kerry J. Abrams, Vikas Kumar, Martina Azzolini, Nicola M. Pugno, Maurizio Dapor, Andreas Huber, Philip Schäfer, David G. Lidzey, and Cornelia Rodenburg*

Understanding nanoscale molecular order within organic electronic materials is a crucial factor in building better organic electronic devices. At present, techniques capable of imaging molecular order within a polymer are limited in resolution, accuracy, and accessibility. In this work, presented are secondary electron (SE) spectroscopy and secondary electron hyperspectral imaging, which make an exciting alternative approach to probing molecular ordering in poly(3-hexylthiophene) (P3HT) with scanning electron microscope-enabled resolution. It is demonstrated that the crystalline content of a P3HT film is reflected by its SE energy spectrum, both empirically and through correlation with nano-Fourier-transform infrared spectroscopy, an innovative technique for exploring nanoscale chemistry. The origin of SE spectral features is investigated using both experimental and modeling approaches, and it is found that the different electronic properties of amorphous and crystalline P3HT result in SE emission with different energy distributions. This effect is exploited by acquiring hyperspectral SE images of different P3HT films to explore localized molecular orientation. Machine learning techniques are used to accurately identify and map the crystalline content of the film, demonstrating the power of an exciting characterization technique.

1. Introduction


A growing body of recent work has established the modern field of secondary electron (SE) energy spectroscopy.^[1–5] This technique in the scanning electron microscope (SEM) has enabled fresh, exciting insights in to the properties of polymeric, organic, and biological materials by exploiting the relationship between the emitted SE energy distribution and various material properties. By performing energy-selective detection of SEs in the SEM, techniques such as secondary electron hyperspectral imaging (SEHI) have been used to form images which can map nanoscale variations in chemistry or molecular ordering.^[3,4]

To date, studies applying SE energy spectroscopy principles have largely been based upon empirical relationships between the SE spectrum and sample features. We have demonstrated that such empirical studies are sufficient to underpin many powerful

Dr. R. C. Masters, N. Stehling, Dr. K. J. Abrams, Dr. V. Kumar,
Dr. C. Rodenburg
Department of Materials Science and Engineering
University of Sheffield
Sheffield S1 3JD, UK
E-mail: c.rodenburg@sheffield.ac.uk

Dr. M. Azzolini, Prof. M. Dapor
European Centre for Theoretical Studies in Nuclear Physics
and Related Areas (ECT*-FBK) and Trento Institute for Fundamental
Physics and Applications (TIFPA-INFN)
Trento 38123, Italy

Dr. M. Azzolini, Prof. N. M. Pugno
Laboratory of Bio-Inspired and Graphene Nanomechanics
Department of Civil
Environmental and Mechanical Engineering
University of Trento
Trento 38123, Italy

 The ORCID identification number(s) for the author(s) of this article can be found under <https://doi.org/10.1002/adv.201801752>.

© 2019 The Authors. Published by WILEY-VCH Verlag GmbH & Co. KGaA, Weinheim. This is an open access article under the terms of the Creative Commons Attribution License, which permits use, distribution and reproduction in any medium, provided the original work is properly cited.

DOI: 10.1002/adv.201801752

Prof. N. M. Pugno
Ket-Lab
Edoardo Amaldi Foundation
Rome 00133, Italy

Prof. N. M. Pugno
School of Engineering and Materials Science
Queen Mary University of London
London E1 4NS, UK

Dr. A. Huber, Dr. P. Schäfer
Neaspec GmbH
Bunsenstrasse 5, 82152 Planegg, Germany

Prof. D. G. Lidzey
Department of Physics and Astronomy
University of Sheffield
Sheffield S3 7RH, UK

applications of SEHI. However, delivering fully on the potential of SEHI, as a characterization technique, requires a robust understanding of the nature of SE spectra and the ability to link spectral features with specific sample properties. Developing these links is a complex task.

SE emission in the SEM results from a “cascade” of electron-sample interactions initiated by the primary electron beam. SEs generated within the material may each interact multiple times with sample atoms, electrons, phonons, and trap sites.^[6] Every interaction can influence the angle and energy of an emitted SE, and as such, the energy distribution of emitted SEs results from a complex convolution of various material and electronic properties. Peaks in the SE spectrum have been linked with the energy levels of conduction band minima in graphite^[7,8] as well as the nanoscale bonding structure in organic materials.^[9] The effect of sample doping on the spectrum shape is also well documented.^[10,11] However, building a deeper understanding of the origin of SE spectral features will unlock new analytical capabilities, for example in using a sample’s SE spectrum to probe and map its electronic or chemical properties directly.

In this work, we systematically investigate the sample properties that influence the SE spectrum of a polymer, and in doing so provide a powerful example of the potential capabilities of SEHI. We use the technique to investigate and map molecular ordering in poly(3-hexylthiophene) (P3HT), a semicrystalline polymer with a range of organic electronic applications.^[12] Localized molecular ordering in a P3HT film is a crucial aspect determining its electronic properties,^[13–16] as the electron transport through a bulk film is defined by the nature and interconnectivity of its crystalline domains.^[17] More broadly, the importance of localized molecular order is observed across many polymer science applications, from organic photovoltaics^[18] to drug-delivery systems.^[19] By probing the nature of ordering with SEM-level resolution, we demonstrate a compelling new characterization tool which can aid development and understanding of a range of new materials.

We forge links between the molecular order of P3HT films and the SE spectrum using both an experimental approach and an advanced Monte Carlo modeling technique.^[2] We identify the sample properties that have the strongest influence on the shape of the SE spectrum, and explore how this spectrum relates to molecular ordering. Further, we apply SEHI methods to map molecular ordering across P3HT samples for the first time. Hyperspectral SE maps of P3HT films are analyzed with advanced spectral decomposition methods, powered by machine-learning, to map the relative fraction of amorphous and crystalline material across the surface of P3HT with <100 nm resolution. As a result, we demonstrate SEHI as a robust, analytical microscopy technique that can dramatically expand the capabilities of the modern-day SEM.

2. Results and Discussion

2.1. Secondary Electron Energy Spectroscopy

In **Figure 1**, we present SE energy spectra measured from two different types of P3HT films, which we define as amorphous and semicrystalline. These are terms of convenience for this

work, albeit not entirely accurate descriptors for the different types of film. The amorphous film was processed from regiorandom P3HT, whereby the random orientation of side-chains acts to inhibit crystallite formation.^[14,20] Regiorandom films are predominantly homogeneous and amorphous.^[21] In contrast, the semicrystalline film was processed from highly regioregular P3HT using a high-boiling point solvent and subsequently treated with a thermal anneal. This encourages the formation of crystalline phases within the film alongside a considerable amorphous fraction.^[17,21] Our full sample preparation methods are included in the Supporting Information for this work.

Secondary electron spectra measured from the different P3HT films in a FEI Sirion SEM are presented in **Figure 1a**. The experimental methods used to acquire and process these data can be found in the Supporting Information. The spectra in **Figure 1a** were acquired with a total dose of $\approx 3.4 \times 10^{13}$ electrons cm^{-2} . While the spectra have broadly the same form, some notable differences can be observed resulting from different levels of molecular ordering. First, around 1 eV, the semicrystalline P3HT sample is seen to have two peaks (peaks 1 and 2, denoted by arrows) where the amorphous P3HT sample has only one. Second, a higher energy peak around 3 eV (peak 3, denoted by an arrow) has higher intensity in the semicrystalline P3HT sample. We attribute these differences to the crystalline phases in the semicrystalline sample. These results were consistently reproduced from at least five different P3HT samples of each type measured over >1 year, with the shaded regions in **Figure 1a** demonstrating the standard error on spectra measured from three different areas of the same sample, spaced by $\approx 500 \mu\text{m}$. With no significant location-dependent variation observed in these data, we assume that wide field spectra are representative of the bulk properties of the sample.

2.2. Localized Variation in SE Spectra

To explore the contribution of localized molecular order in the SE spectrum emitted from P3HT, SE spectra were measured from different areas $\approx 60 \text{ nm}^2$ in size, using a modern Helios Nanolab SEM. Due to the smaller measurement area, these spectra were acquired with a total electron dose of 2.16×10^{15} electrons cm^{-2} , almost two magnitudes larger than that used to acquire SE spectra in **Figure 1a**. As such, SE spectra in **Figure 1c** (amorphous) and **Figure 1f** (semicrystalline) are susceptible to the effects of charging and electron beam damage, which results in these spectra having a slightly different form and peak positions in comparison to **Figure 1a**. However, the important molecular order related SE spectral features observed in **Figure 1a** are still present in **Figure 1f** (denoted by arrows). We assume these features are equivalent with those identified in **Figure 1a** and thus have the same origin.

Example SE spectra measured from 60 nm^2 areas are presented in **Figure 1c** (amorphous) and **Figure 1f** (semicrystalline). Here, these small-area spectra, plotted with colored lines, are compared with larger ($\approx 2 \mu\text{m}^2$) measurement area spectra, plotted with a thicker black line. We observe that in **Figure 1f**, the localized variation in SE spectra is significant. Specifically, the relative intensity of peaks 1, 2, and 3 in **Figure 1f** appear to fluctuate across the sample surface. To separate the influence of

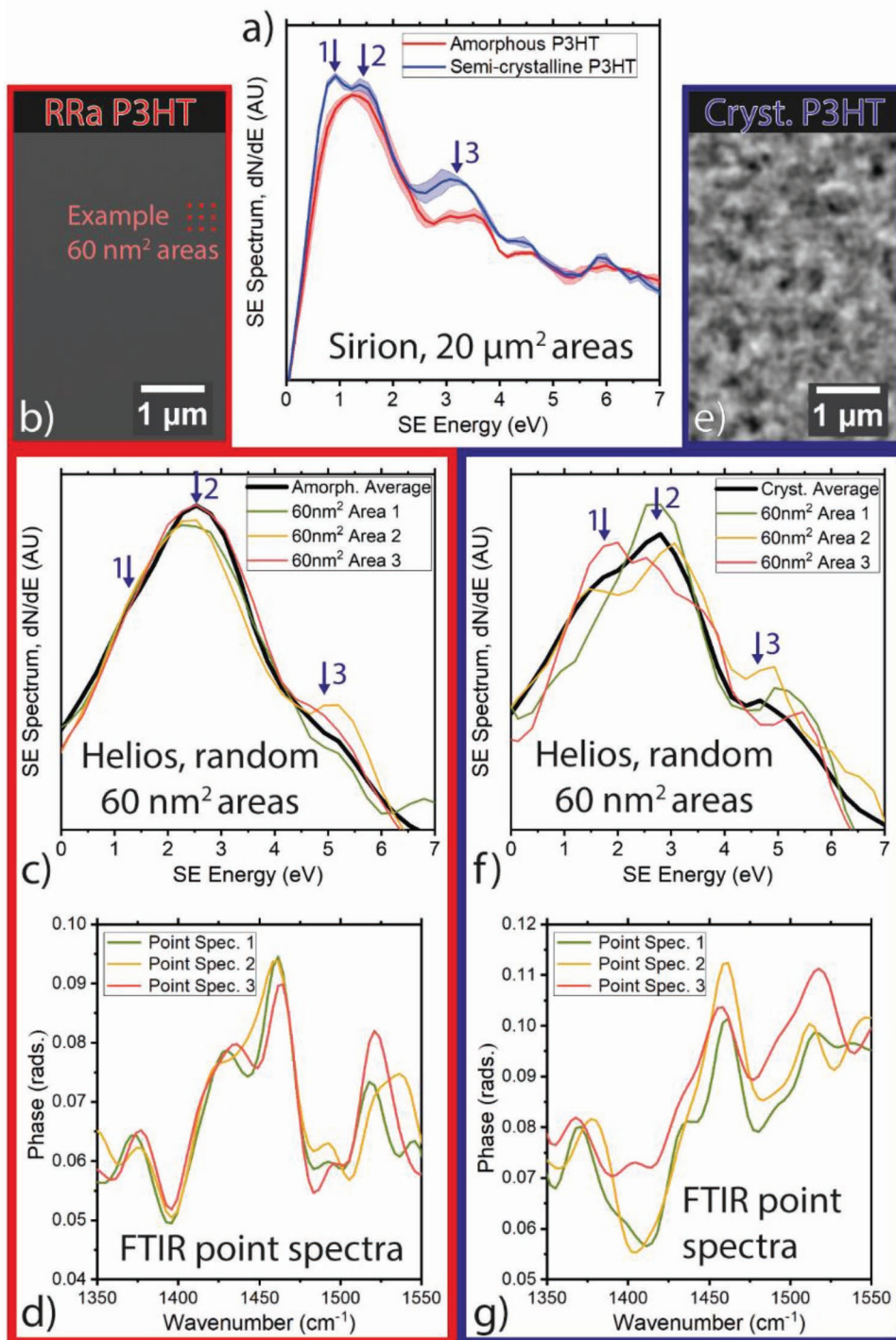


Figure 1. Secondary electron spectroscopy of P3HT, localized chemical variation. a) Compares low-magnification SE spectra of amorphous and semi-crystalline P3HT, measured from $20 \mu\text{m}^2$ areas in the FEI Sirion SEM. b–d) Consider localized variation in amorphous (regiorandom) P3HT films. b) Shows a conventional SEM image of the film, and c) shows SE spectra measured from 60 nm^2 areas in the FEI Helios SEM. The scale of these measurement areas is depicted by red squares in (b). d) Shows nano-FTIR point spectra measured from random areas on the film. e–g) Similarly consider localized variation in a semicrystalline P3HT film. e) Shows a SEM image of a semicrystalline film and f) shows SE spectra measured from random 60 nm^2 areas of the film in the FEI Helios SEM. g) Shows nano-FTIR point spectra measured from random areas of a semicrystalline P3HT film.

molecular order on the SE spectra from any potential localized charging or shot noise effects on peak position or total spectrum intensity we compare the variations in relative intensities

between peaks 1 and 2. For the semicrystalline sample, we find a standard deviation of $\approx 14\%$ around the mean for ≈ 2500 spectra. This suggests that the SE transport and/or emission

properties of the semicrystalline P3HT film are heterogeneous on the scale of tens of nanometers. In contrast the amorphous P3HT film is more homogeneous, as evidenced by the smaller variation in SE spectra in Figure 1c. The intensity of peak 1 relative to that of peak 2 for the same spectrum showed a standard deviation of $\approx 9\%$ for this sample (≈ 2500 spectra). This greater homogeneity is in line with the lack of observable features in the SE image of this sample (Figure 1b). These observations suggest a link between molecular ordering and the fine structure in the SE spectra. Directly corroborating this link is difficult with established techniques. However, here we apply experimental and modeling techniques to further establish the connection. One established technique known to reflect local molecular order is Fourier-transform infrared spectroscopy (FTIR).

2.3. Nano-FTIR: Localized Chemical Variation

Nano-FTIR enables the chemical properties of P3HT films to be analyzed on the nanoscale, allowing the correlation of localized variation in sample chemistry with variation in SE spectra (methods described in the Supporting Information). In Figure 1d,g, we compare nano-FTIR spectra measured from different areas of semicrystalline and amorphous P3HT samples. Specifically we consider the symmetric C–C and antisymmetric C=C stretching modes measured here at 1460 and 1520 cm^{-1} respectively.^[22] The intensity ratio between the 1460 and 1520 cm^{-1} peaks, I_{1460}/I_{1520} , reflects the effective conjugation length of the film at the measured point^[23] and has been strongly linked to molecular ordering and electron mobility in the film.^[23,24]

In Figure 1g, significant variation in the different point spectra can be observed, reflecting variation in the localized chemistry of the semicrystalline film. The I_{1460}/I_{1520} ratio of different point spectra is seen to fluctuate by $\approx 10\%$ around the average reflecting localized variation in ordering and electron transport through the film. This correlates with the nature the narrow-field SE spectra in Figure 1f.

Considering the amorphous P3HT film, we note that both the narrow-field SE spectra (colored plots in Figure 1c) and nano-FTIR point spectra (Figure 1d) demonstrate only small variations across the sample. This is consistent with the picture of regiorandom P3HT films in literature.^[21] The I_{1460}/I_{1520} ratio of the point spectra in Figure 1d is around 1.3, with this larger value indicating shorter conjugated polymer segments on average in comparison to the semicrystalline sample. However, one nano-FTIR point spectrum (plotted in orange) in Figure 1d shows clearly different form in comparison to the others, and a I_{1460}/I_{1520} ratio of 1.1 indicating a greater average conjugation length. This indicates that areas with stronger molecular ordering are nonetheless present in the regiorandom film, an effect that has been previously observed.^[21] Evidence of localized ordering in the amorphous film is also present in narrow-field SE spectra, as discussed further below in relation to Figure 3c.

Combining localized SE spectra with the results acquired with nano-FTIR, localized variation in SE spectroscopy appears to correlate with localized variation in molecular ordering. This

strengthens the correlation we find between peaks 1 and 3 in the P3HT SE spectrum and crystalline content in the film. In order to exploit this effect for local crystallinity mapping we first consider the effect of the electron beam exposure on the crystallinity.

2.4. Electron Beam Dose Effects on Secondary Electron Spectrum

P3HT films are well known to be susceptible to electron beam damage,^[25,26] with loss of molecular ordering being one of the damage effects occurring at lowest dose.^[25] In Figure 2, we consider how the measured P3HT SE spectrum is affected by the electron dose and dose rate.

In Figure 2a, we present the effect of increasing electron dose on the SE spectrum measured from $\approx 10 \mu\text{m}^2$ areas of a semicrystalline P3HT sample in the Helios SEM. Up to at least an acquisition dose of 2.16×10^{15} electrons cm^{-2} , the characteristic low-energy peak demonstrated by semicrystalline P3HT films (peak 1 in Figure 1f) is visible. However, for a spectrum acquisition dose of 4.32×10^{15} electrons cm^{-2} , this peak is observed to have decreased significantly in intensity, such that the spectrum appears to resemble that of an amorphous P3HT film (black plot, Figure 2a). We found the SE spectrum of the amorphous P3HT sample however appears to be largely unchanged for electron doses up to 5×10^{15} electrons cm^{-2} .

A recent study^[26] demonstrated that loss of molecular ordering in P3HT occurred with critical electron doses of $< 2 \times 10^{15}$ electrons cm^{-2} (albeit in the transmission electron microscope (TEM)). Therefore, we suggest that the degradation of the low-energy peak in Figure 2a with increasing dose is related to the destruction of molecular ordering in the film. This further strengthens the link between peak 1 in Figure 1a,f and the crystalline content of the film.

Comparing the SE spectra in Figure 2a,b shows the importance of not only electron beam dose in SE spectrum acquisition, but also the pattern in which this dose is delivered. In Figure 2a, electron beam parameters were specifically selected to demonstrate beam damage effects (Supporting Information). In Figure 2b, we used the same electron beam scan pattern to that used to acquire the spectra in Figure 1c,f: a short 50 ns dwell time coupled with frame-integration (each pixel was irradiated in 50 ns pulses, with a ≈ 20 ms delay between successive irradiation events). For both parts of Figure 2, an identical electron beam current was used.

In Figure 2b, the 7.22×10^{15} electrons cm^{-2} spectrum acquired with short dwell-time and frame integration retains the clear low-energy peak as expected from a semicrystalline sample. This contrasts the 4.32×10^{15} electrons cm^{-2} dose spectrum in Figure 2a, where, when measured with a lower dose but longer dwell time, the SE spectrum suggests sample damage. We expect that the short dwell time employed in Figure 2b minimizes the number of electrons excited by a single “pulse” of electron beam irradiation, and the long delay between subsequent irradiation events in the frame integration scan pattern allows time for excited electrons to relax to a lower-energy state before repeated exposure occurs. This minimizes chemical damage to the sample.^[27,28]

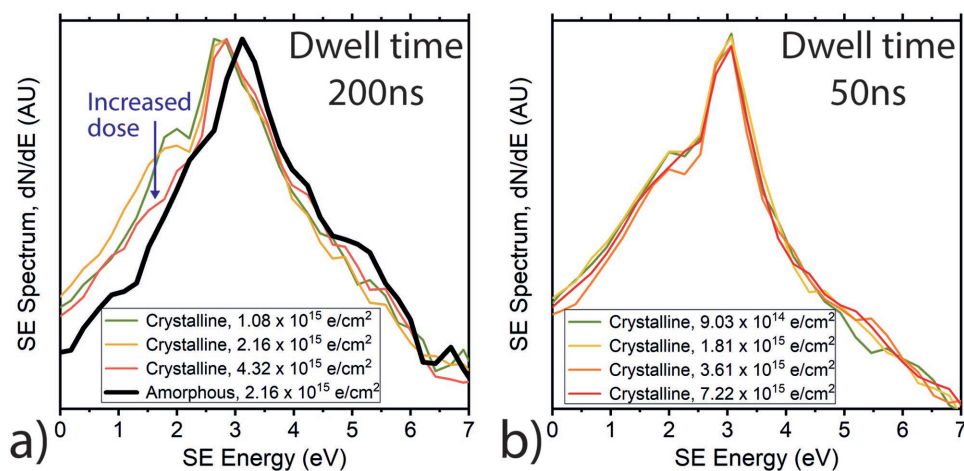


Figure 2. Effect of electron dose on the experimentally measured SE spectrum, from $\approx 10 \mu\text{m}^2$ areas. a) Effect of increasing dose with 200 ns dwell time and increasing line integrations. b) Effect of increasing dose with 50 ns dwell time and increasing frame integrations.

Figure 2a suggests that SEHI techniques may have limitations when studying some highly beam-sensitive samples, for which spectrum acquisition doses may exceed a critical dose for loss of molecular order. Similar effects are observed when studying beam-sensitive materials with many analytical electron microscopy techniques.^[29] Understanding and accounting for potential beam damage effects is therefore crucial to any reliable SEHI study. Yet, electron dose and dose rate induced spectral changes can be used to assess whether an image obtained with a particular dose and dose rate are representative of the original material or of heavily beam damaged material.

For P3HT, Figure 2b shows that beam damage effects can be mitigated using advanced beam scanning methods, allowing localized SE spectrum acquisition from areas $\approx 60 \text{ nm}$ across. The electron dose effect on the P3HT spectrum further supports the link between peak 1 (as defined in Figure 1) and the presence of crystalline material in the measurement area. Based upon this link, we apply SE hyperspectral imaging to map molecular ordering in P3HT, using machine-learning powered techniques.

2.5. Secondary Electron Hyperspectral Imaging with Machine Learning: Mapping Molecular Ordering at the Surface

We used techniques demonstrated above to produce SE hyperspectral maps of P3HT samples. Non-negative matrix factorization (NMF) techniques were used to determine the principal components causing variation in the SE spectrum across the surface of our samples. These techniques were applied using the Hyperspy software package to SEHI maps of multiple P3HT samples, as described fully in the Supporting Information.

In Figure 3a, we show the two dominant spectrum factors output by the NMF decomposition algorithm. The two factors can be closely related to SE spectral features emitted from crystalline and amorphous phases. component 1 (in red) is a broad, featureless peak resembling the SE spectrum measured from amorphous P3HT in the Helios SEM (Figure 1c), with peak position at a similar energy to peak 2 as defined in Figure 1c,f.

component 2 (in blue) does not resemble a SE spectrum when considered independently. However, component 2 demonstrates peaks at ≈ 1 and $\approx 4 \text{ eV}$, in positions similar to those of peaks 1 and 3 (as defined in Figure 1c,f), which we have linked to the presence of molecular ordering in this work. We therefore model the spectral decomposition results as reflecting the spectrum of an amorphous matrix (represented by component 1), having additional peaks when crystalline material is present (represented by convoluting components 1 and 2)

In Figure 3b, we combine components 1 and 2 in different ratios, to model the appearance of a SE spectrum consisting of different relative loadings of components 1 and 2. For low relative component 2 loadings, the modeled spectrum resembles the experimental spectrum measured from the amorphous P3HT film. The decomposition model best matches the amorphous P3HT spectrum with around $\approx 20\%$ component 2 loading, with a small shoulder around the position of peak 1 (as defined in Figure 1c). Further, we observe that, for small component 2 loadings, varying the relative loading of component 2 in the modeled spectrum produces only small variation in the SE spectrum. This reflects the small degree of variation in the narrow-field SE spectra of this sample (Figure 1c). With higher component 2 loadings, peaks 1 and 3 (as defined in Figure 1c,f) become more prominent; we observed the same effect in experimental spectra measured from samples containing higher crystallinity. This is demonstrated in Figure 3c. At component 2 loadings of $\approx 40\%$, the modeled spectrum is an excellent match to the experimental SE spectrum of the semicrystalline sample as measured in the Helios SEM (Figure 1f).

In Figure 3d, we map the relative strength of components 1 and 2 across amorphous and semicrystalline P3HT samples. Component 1 demonstrates strong loadings across both P3HT samples. For the amorphous sample, the component 1 loading is high for the large majority of the image (mean loading of $\approx 90\%$, 97% of the map is above $\approx 80\%$ loading), reflecting the strong link between component 1 and amorphous material. In the semicrystalline sample, a lower average component 1 loading of $\approx 75\%$ is present. This reflects the presence of significant crystalline phases alongside some highly amorphous

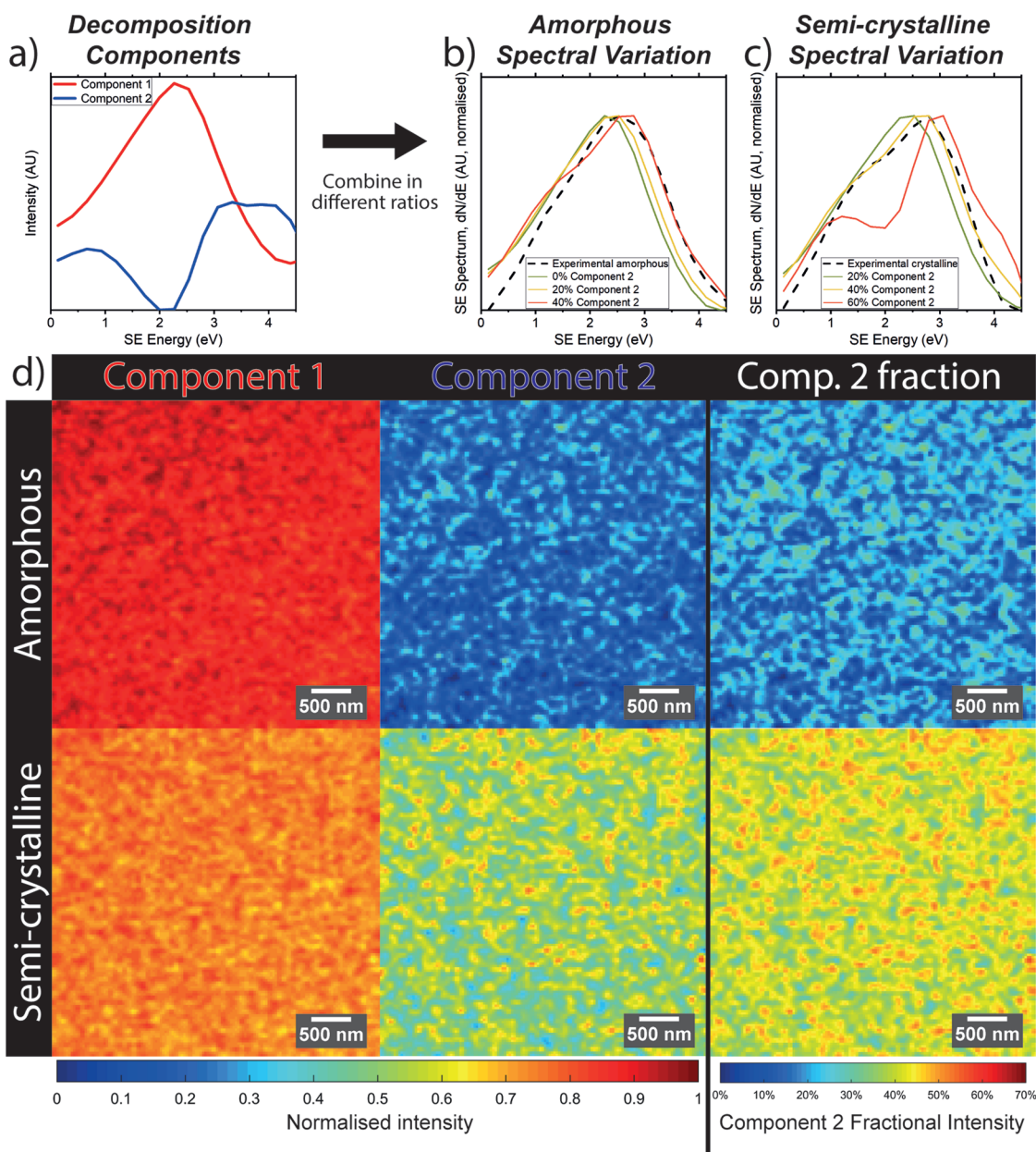


Figure 3. SEHI study of amorphous and semicrystalline P3HT with NMF spectral decomposition. a) Shows the two major components factorized from P3HT SE spectra. b,c) Show how these components form localized SE spectral variation when combined in different fractions, as compared to experimental spectra measured from amorphous and semicrystalline samples. d) Shows the spatially resolved relative loadings of these two spectral components across the sample surface of amorphous and semicrystalline P3HT films, as well as a map of the spatially resolved relative intensity of component 2 as a fraction of total spectrum intensity

regions up to ≈ 100 nm across ($\approx 15\%$ of the map has loading above 80%). Both amorphous and semicrystalline samples show similar standard deviation in component 1 loading, around 4%. This suggests that the amorphous component is fairly consistent for both materials. Regarding component 2, we find the semicrystalline sample to have a mean loading of $\approx 60\%$ with a standard deviation of $\approx 11\%$ across the SEHI map. This compares with the amorphous sample, having a mean loading of $\approx 20\%$ with standard deviation around 9%. This reflects a more amorphous and homogenous sample and is expected;

however, the difference in standard deviation with respect to the semicrystalline sample (11%) is small. This is most likely because component 2 variation has little effect on the shape of the spectrum at the low loadings found in the amorphous sample (effect in Figure 3b), which introduces greater error in the spectral decomposition algorithm.

To visualize SE spectral variation more accurately, the relative fraction of component 2 is also mapped in Figure 3d. Here, where I_n is the localized intensity of NMF component n , the fractional intensity of component 2 is given by $I_2/(I_1 + I_2)$. As

such, the component 2 fractional intensity maps eliminate any localized variation in overall spectrum intensity, possibly influenced by localized topography or charging, and instead reflect only the shape of the localized spectrum. The localized spectrum shape can be defined entirely by the relative fraction of component 2 in a NMF-modeled spectrum, as demonstrated in Figure 3b,c.

For the semicrystalline sample, we show that the fractional loading of component 2 varies considerably between $\approx 25\%$ and 60% across the semicrystalline sample. As demonstrated in Figure 3c, larger average component 2 loadings give rise to peaks 1 and 3 as denoted in Figure 1. Figure 3d suggests that while every 60 nm pixel in the SEHI map of the semicrystalline film contains some degree of crystallinity, the relative fraction of localized crystallinity varies considerably across the sample. This is in agreement with literature, where molecular-scale aggregates and larger-scale crystallites have been shown to co-exist with amorphous phases.^[17] Highly ordered phases in the component 2 fraction map in Figure 3d measure around 100–200 nm in size, and are closely intermixed with more amorphous phases, as expected from more recent models of the P3HT system.^[17] The length-scale matches well with atomic force microscope maps of similar P3HT films,^[30] as well as some P3HT structures within similarly processed blend films that we have previously imaged with a higher-resolution SEM technique.^[4] It is important to note however that the morphology of P3HT is hierarchical,^[31] and in Figure 3 we only map morphology on a length scale limited by resolution due to electron dose with the current experimental setup.

In the fractional component 2 map of the amorphous sample, we observe that the regiorandom amorphous sample shows various regions containing up to $\approx 30\%$ or even greater fractional loading of component 2. The presence of some regions of higher component 2 loading indicates some limited, localized molecular ordering in a sample that is often depicted as uniformly amorphous. This effect was previously detected,^[21] with small regioregular segments even in a “perfect” regiorandom molecule enabling the formation of small crystallites. These are small enough to be “invisible” to many characterization techniques such as wide-angle X-ray scattering;^[21] however, our localized SE spectra suggest at their presence here. We detect areas 200–300 nm across containing

a component 2 (crystalline) fraction $>20\%$, alongside similar-sized areas having negligible component 2 loading (i.e., almost entirely amorphous).

Figure 3 depicts a technique with strong potential for mapping localized sample properties in a rapid, easily implemented way. The acquisition of a full SEHI map takes just ≈ 2 min using an automated acquisition script on an unmodified SEM. However, the spatial and energy resolution of this technique is limited by electron dose effects. Image magnification (i.e., pixel resolution) and acquisition time (i.e., signal-to-noise ratio) were limited in order to acquire the SEHI maps in Figure 3d without incurring the beam damage effects presented in Figure 2. It is known, for example, that smaller crystalline structure than that visible in Figure 3 is present in P3HT films.^[32] We expect that this dose-limited resolution could be improved significantly with advances in hardware, for example with more advanced SE spectrometers.^[1]

Figure 3 demonstrates how the links between molecular order and SE spectral features suggested in Figures 1 and 2 may be employed to map material properties. However, in order to apply the technique more broadly and confidently, we investigate the fundamental origin of these SE spectral features more closely from a theoretical standpoint.

2.6. Monte Carlo Modeling of the SE Spectrum

We simulated the shape of the P3HT SE spectrum from a Monte Carlo model of the physical processes and interactions resulting from a primary electron beam impinging on a P3HT film. An overview of the modeling methods used is included in the Supporting Information to this work; however, the main input parameters are the complex dielectric function, and the electron affinity (χ). As the electron affinity is closely linked to electronic dipoles at the surface, and hence to molecular order and orientation,^[33] below we present the results, showing the effect of different electron affinities on the spectra.

The accuracy of the simulation for this work was verified by modeling the SE spectrum of an amorphous P3HT film (Figure 4a). Amorphous P3HT is an ideal test case for this purpose; electron transport in an amorphous film is simpler

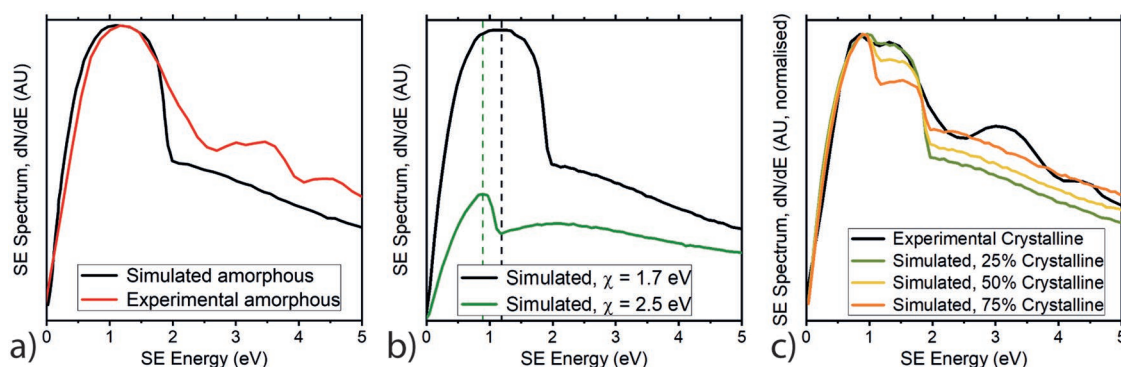


Figure 4. Monte Carlo modeling of secondary electron spectra. a) Comparison of experimental and simulated spectra for amorphous P3HT. b) Effect of changing the electron affinity parameter in Monte Carlo simulation of SE spectrum. c) Simulating the SE spectrum of a semicrystalline P3HT film by considering the different electronic properties of amorphous and crystalline phases.

to model due to its relative homogeneity.^[2] We compared the modeled spectra with experimental spectra measured in the FEI Sirion tool (Figure 1a). The modeled spectrum demonstrates two primary features: a large, dominant peak at low energies (<2 eV), with a long tail at higher energies. This produces a good match for the general shape of the experimental spectrum.

In Figure 4b, we explore the effect of electron affinity on the SE spectrum shape. The values of P3HT electron affinity in literature take a range of values, from 2.1^[14] to 3.2 eV,^[34] as such the χ values modeled in Figure 4b ($\chi = 1.7$ and 2.5 eV) are a reasonable match to real P3HT films. We observe that with a higher electron affinity value, the SE spectrum drops considerably in overall intensity, and the low-energy peak becomes narrower and less intense relative to the tail. This reflects electron affinity as an analogue for the energy barrier that an internal SE must overcome if it is to be emitted. A larger electron affinity therefore has the effect “cutting-off” low-energy SEs from the emitted spectrum, and “compressing” the low-energy peak into a smaller energy range. At higher electron affinities, the higher-energy spectral feature that is observed as a tail for $\chi = 1.7$ eV is revealed to be a peak at ≈ 2 eV in the $\chi = 2.5$ eV spectrum. The energy position of this feature appears independent of the electron affinity value, suggesting it may be representative of some other feature of the sample.

In Figure 4c, the effect of different electron affinity values on the SE spectrum shape is used to explain the “double” peak feature observed around 1 eV in the wide-field SE spectrum of semicrystalline P3HT (Figure 1a). We model the semicrystalline P3HT film as a two-phase system consisting of domains of different electron affinity. A SE can then be emitted from an area of the film with one of two electron affinity values. By setting the electron affinities of these two phases to $\chi = 1.7$ and 2.5 eV respectively, our modeled P3HT spectrum accurately recreates the double-peak feature around 1 eV (peaks 1 and 2 in Figure 1a). As the semicrystalline P3HT sample emits a SE peak at lower energies than the amorphous sample in all of our experimental SE spectra (Figures 1 and 2), we ascribe an average $\chi = 2.5$ eV to the crystalline phase, and an average $\chi = 1.7$ eV to the amorphous phase. P3HT films with a greater degree of molecular ordering have a larger bulk electron affinity in literature.^[33] The difference in the electron affinity we model from crystalline and amorphous domains relates to localized variation that is typically averaged by conventional bulk measurements of χ .

The relative intensities of the two low-energy peaks in Figure 4c can be used to infer the fraction of the sample surface consisting of each domain. Matching the semicrystalline SE spectrum in Figure 1a to this data, we approximate from our data that $\approx 25\%$ of the semicrystalline P3HT film surface is crystalline. The absolute crystallinity content of P3HT films is difficult to compare with literature due to the effects of surfaces and interfaces on the absolute values.^[21] However we note that this crystallinity value is significantly smaller than that measured from bulk samples of comparable molecular weight and regioregularity ($\approx 50\%$) using X-ray scattering and nuclear magnetic resonance methods.^[21] This is expected for a spin-cast film.^[21] We also investigated the role of differences in the complex dielectric function but find a very weak influence (see Supporting Information)

Our findings here are an important demonstration that bulk electronic measurements perhaps generate a simplified picture of a nanostructured film, where crystalline and amorphous phases demonstrate significantly different electronic properties.^[17] As electronic devices shrink to ever smaller sizes, considering these nanoscale variations will be of increasing importance.

3. Conclusion

In this work, we have delivered important advancements in SE spectroscopy and SEHI, both building upon and underpinning our previous work to showcase a characterization technique with real potential. We demonstrated that specific spectral features correlate with crystalline content in the film, through both empirical study of experimental spectra and from a theoretical standpoint with a Monte Carlo modeling technique. Further, by comparing our SE spectroscopy results with a study of nanoscale chemistry through nano-FTIR, we showed that localized variation in P3HT SE spectra matches well with localized variation in conjugation length, an indicator of molecular order.

By modeling the P3HT SE spectrum, we showed that the spectral features can be related to the localized electronic properties of the film. These electronic properties are themselves associated with localized molecular ordering. We found that the electron affinity of the sample is a dominant factor determining the shape of the spectrum.

Finally, we demonstrated SEHI, combined with data analysis powered by machine learning, as a tool for mapping localized molecular order in P3HT with 60 nm² pixel size. Our SEHI techniques can be applied on various modern SEM systems with no hardware modification, with data acquisition performed in ≈ 2 min and no extraordinary sample preparation required.

We anticipate that in time, advancements in detector hardware will enable even higher resolution SEHI maps of beam sensitive materials. In the meantime, relevant implementations of low-dose TEM methods, such as advanced denoising or compressed sensing,^[35,36] may enable further progress. We expect that with further advancements such as these, SE energy spectroscopy and SEHI techniques can develop in to standalone, powerful, and versatile materials characterization tools that exploit the power of the modern-day SEM to its fullest extent.

Supporting Information

Supporting Information is available from the Wiley Online Library or from the author.

Acknowledgements

R.M., N.S., K.A., V.K., and C.R. thank the UK Engineering and Physical Sciences Research Council (EPSRC) for supporting this work under Grant EP/N008065/1 “SEE MORE: Secondary Electron Emission—Microscopy for Organics with Reliable Engineering-Properties.” D.G.L. and C.R. also thank the EPSRC for support via Grant EP/M025020/1 “High resolution mapping of performance and degradation mechanisms in printable photovoltaic devices.” The authors also thank the Leverhulme Trust for

funding a collaboration between C.R. and M.D. The authors gratefully acknowledge the Gauss Centre for Supercomputing for funding this project by providing computing time on the GCS Supercomputer JUQUEEN at Juelich Supercomputing Centre (JSC).^[37] Furthermore, the authors acknowledge FBK for providing unlimited access to the KORE computing facility. N.M.P. was supported by the European Commission under the Graphene Flagship Core 2 Grant No. 785219 (WP14, “Composites”) and FET Proactive (“Neurofibres”) Grant No. 732344 as well as by the Italian Ministry of Education, University and Research (MIUR) under the “Departments of Excellence” Grant L.232/2016.

Conflict of Interest

The authors declare no conflict of interest.

Keywords

electron microscope, molecular order, organic electronics, polymer, secondary electron spectroscopy

Received: October 19, 2018

Revised: December 8, 2018

Published online:

- [1] N. Stehling, R. Masters, Y. Zhou, R. O’Connell, C. Holland, H. Zhang, C. Rodenburg, *MRS Commun.* **2018**, *8*, 226.
- [2] M. Dapor, R. C. Masters, I. Ross, D. G. Lidzey, A. J. Pearson, I. Abril, R. Garcia-Molina, J. Sharp, M. Unčovský, T. Vystavel, F. Mika, C. Rodenburg, *J. Electron Spectrosc. Relat. Phenom.* **2017**, *222*, 1.
- [3] Q. Wan, K. J. Abrams, R. C. Masters, A. C. S. Talari, I. U. Rehman, F. Claeysens, C. Holland, C. Rodenburg, *Adv. Mater.* **2017**, *29*, 1703510.
- [4] R. C. Masters, A. J. Pearson, T. S. Glen, F.-C. Sasam, L. Li, M. Dapor, A. M. Donald, D. G. Lidzey, C. Rodenburg, *Nat. Commun.* **2015**, *6*, 6928.
- [5] V. Y. Mikhailovskii, Y. V. Petrov, O. F. Vyvenko, *J. Surf. Invest.: X-Ray, Synchrotron Neutron Tech.* **2015**, *9*, 196.
- [6] M. Dapor, *Transport of Energetic Electrons in Solids*, Springer, Berlin **2014**.
- [7] R. F. Willis, B. Feuerbacher, B. Fitton, *Phys. Rev. B* **1971**, *4*, 2441.
- [8] R. F. Willis, B. Feuerbacher, B. Fitton, *Phys. Lett. A* **1971**, *34*, 231.
- [9] K. J. Abrams, J. S. Schaefer, F. Mika, C. Rodenburg, *Electron Microscopy and Analysis Group Conf.* **2018**, p. 48.
- [10] P. Kazemian, S. A. M. Mentink, C. Rodenburg, C. J. Humphreys, *J. Appl. Phys.* **2006**, *100*, 054901.
- [11] I. Volotsenko, M. Molotskii, Z. Barkay, J. Marczewski, P. Grabcic, B. Jaroszewicz, G. Meshulam, E. Grunbaum, Y. Rosenwaks, *J. Appl. Phys.* **2010**, *107*, 014510.
- [12] B. Park, A. Aiyar, J.-I. Hong, E. Reichmanis, *ACS Appl. Mater. Interfaces* **2011**, *3*, 1574.
- [13] L. Biniek, S. Pouget, D. Djurado, E. Gonthier, K. Tremel, N. Kayunkid, E. Zaborova, N. Crespo-Monteiro, O. Boyron, N. Leclerc, S. Ludwigs, M. Brinkmann, *Macromolecules* **2014**, *47*, 3871.
- [14] K. Kanai, T. Miyazaki, H. Suzuki, M. Inaba, Y. Ouchi, K. Seki, *Phys. Chem. Chem. Phys.* **2010**, *12*, 273.
- [15] U. Bielecka, P. Lutsyk, K. Janus, J. Sworakowski, W. Bartkowiak, *Org. Electron. Phys. Mater. Appl.* **2011**, *12*, 1768.
- [16] C. Scharsich, R. H. Lohwasser, M. Sommer, U. Asawapirom, U. Scherf, M. Thelakkat, D. Neher, A. Köhler, *J. Polym. Sci., Part B: Polym. Phys.* **2012**, *50*, 442.
- [17] R. Noriega, J. Rivnay, K. Vandewal, F. P. V Koch, N. Stingelin, P. Smith, M. F. Toney, A. Salleo, *Nat. Mater.* **2013**, *12*, 1038.
- [18] T. Heumueller, W. R. Mateker, I. T. Sachs-Quintana, K. Vandewal, J. A. Bartelt, T. M. Burke, T. Ameri, C. J. Brabec, M. D. McGehee, *Energy Environ. Sci.* **2014**, *7*, 2974.
- [19] F. Alexis, *Polym. Int.* **2005**, *54*, 36.
- [20] K. Tremel, S. Ludwigs, *P3HT Revisited—From Molecular Scale to Solar Cell Devices*, Springer, Berlin **2014**, pp. 39–82.
- [21] X. Shen, W. Hu, T. P. Russell, *Macromolecules* **2016**, *49*, 4501.
- [22] D. E. Motaung, G. F. Malgas, C. J. Arendse, S. E. Mavundla, D. Knoesen, *Mater. Chem. Phys.* **2009**, *116*, 279.
- [23] M. Akimoto, Y. Furukawa, H. Takeuchi, I. Harada, Y. Soma, M. Soma, *Synth. Met.* **1986**, *15*, 353.
- [24] A. R. Murphy, P. C. Chang, P. VanDyke, J. Liu, J. M. J. Fréchet, V. Subramanian, D. M. DeLongchamp, S. Sambasivan, D. A. Fischer, E. K. Lin, *Chem. Mater.* **2005**, *17*, 6033.
- [25] H. Ahn, D. W. Oblas, J. E. Whitten, *Macromolecules* **2004**, *37*, 3381.
- [26] Z. J. W. A. Leijten, A. D. A. Keizer, G. de With, H. Friedrich, *J. Phys. Chem. C* **2017**, *121*, 10552.
- [27] Y. Kishimoto, T. Ohshima, M. Hashimoto, T. Hayashi, *J. Appl. Polym. Sci.* **1990**, *39*, 2055.
- [28] A. Charlesby, *Atomic Radiation and Polymers: International Series of Monographs on Radiation Effects in Materials*, Pergamon Press, Oxford **1960**.
- [29] R. F. Egerton, P. Li, M. Malac, *Micron* **2004**, *35*, 399.
- [30] A. Zen, J. Pflaum, S. Hirschmann, W. Zhuang, F. Jaiser, U. Asawapirom, J. P. Rabe, U. Scherf, D. Neher, *Adv. Funct. Mater.* **2004**, *14*, 757.
- [31] J. Rivnay, S. C. B. Mannsfeld, C. E. Miller, A. Salleo, M. F. Toney, *Chem. Rev.* **2012**, *112*, 5488.
- [32] M. Brinkmann, P. Rannou, *Macromolecules* **2009**, *42*, 1125.
- [33] H. Ikeura-Sekiguchi, T. Sekiguchi, *Jpn. J. Appl. Phys.* **2014**, *53*, 02BB07.
- [34] J. C. Nolasco, R. Cabré, J. Ferré-Borrull, L. F. Marsal, M. Estrada, J. Pallarès, *J. Appl. Phys.* **2010**, *107*, 044505.
- [35] R. Leary, Z. Saghi, P. A. Midgley, D. J. Holland, *Ultramicroscopy* **2013**, *131*, 70.
- [36] P. Trampert, F. Bourghorbel, P. Potocek, M. Peemen, C. Schlinkmann, T. Dahmen, P. Slusallek, *Ultramicroscopy* **2018**, *191*, 11.
- [37] M. Stephan, J. Docter, *J. Large Scale Res. Facil.* **2015**, *1*, A1.



Supporting Information

for *Adv. Sci.*, DOI: 10.1002/advs.201801752

Mapping Polymer Molecular Order in the SEM with Secondary Electron Hyperspectral Imaging

*Robert C. Masters, Nicola Stehling, Kerry J. Abrams, Vikas Kumar, Martina Azzolini, Nicola M. Pugno, Maurizio Dapor, Andreas Huber, Philip Schäfer, David G. Lidzey, and Cornelia Rodenburg**

Mapping polymer molecular order in the SEM with secondary electron hyperspectral imaging

Supplementary Information

1. Experimental Methods

Sample Preparation

For semi-crystalline P3HT films, P3HT was purchased from Ossila Ltd. (UK), batch M105 with $M_n = 49500$ and regioregularity = 95.5%, and spin-cast from a 25 mg.ml^{-1} dichlorobenzene solution at 1000 rpm to encourage crystal growth. Films were then thermally annealed at 170°C for 20 minutes. For amorphous P3HT films, regiorandom P3HT (510823) was purchased from Sigma-Aldrich, and spin-cast from a 25 mg.ml^{-1} chlorobenzene solution at 1500 rpm. All solution formulation, spin-casting and annealing processes were performed in a nitrogen glovebox environment. Films were cast on to silicon substrates, cleaned in an ultrasonic bath with Hellmanex solution and isopropanol, and finally treated in UV-ozone for 10 minutes prior to the casting process. All samples were stored under nitrogen, and transported to the electron microscope under vacuum conditions to prevent degradation of the film surface.

Electron microscopy and measurement of SE spectra

All electron microscopy work was performed with a primary beam energy $E_0 = 700 \text{ eV}$, with a beam current around 12 pA . These parameters were optimised to minimise charging and electron beam damage issues. Samples were imaged with the through-the-lens detector with immersion-lens active. Two scanning electron microscopes were used: a FEI Sirion, an older microscope with well-documented SE spectroscopy capabilities[1], [2], and a state-of-the-art Thermo Fisher Helios NanoLab G3 UC capable of sub-nanometre imaging resolution[3] and offering an advanced level of electron beam control for dose minimisation.

For both microscopes, energy filtering of SEs was performed by altering the bias on electrodes within the through lens detector assembly. The exact mechanism of energy filtering is similar but differs slightly for each microscope (an overview of SE energy-filtering strategies is given in reference[4]). SE energy spectra and hyperspectral SE images were acquired by capturing a stack of images of the sample whilst sweeping through a range of TLD electrode bias values (again, a detailed overview is given in references[3], [4]).

For work on the FEI Sirion tool, SE spectra were acquired from $20 \mu\text{m}^2$ areas, with each image in the spectrum stack captured in TV scan mode with 228×228 pixel resolution and 4-fold frame integration. For all localised spectrum measurements in the Helios tool (excepting Figure 2a), SE spectra were acquired from $4.1 \mu\text{m}^2$ areas with a monochromated primary beam, with each image in the spectrum stack acquired using 210×210 pixel resolution, 50 pA dwell-time, 128-fold frame integration, and a scan-interlace of 8. For both microscopes, each SE spectrum stack consisted of 51 images. Our justification for using these parameters is discussed regarding Figure 2. For Figure 2b, the number of frame integrations was varied in order to control the spectrum acquisition dose.

To acquire the spectra in Figure 2a, we used the Helios tool with the same beam current, measurement area and resolution, but with a line-integration scan pattern and a 200ns dwell time per pixel (200ns irradiation ‘pulses’, with a $\sim 0.15\text{ms}$ delay between successive pulses). The number of line integrations was varied in order to control the spectrum acquisition dose.

Comparison of Figure 1a with 1c,f demonstrates that the Helios SEM appears to give lower-intensity peaks at low SE energies in comparison to the FEI Sirion. This is likely a result of the limitations of the Helios SEM as a SE spectrometer, which we have investigated previously [4]

SE spectrum and SEHI data analysis

SE spectra were processed through an in-house MATLAB script to organise and process the spectrum image stack into the spectra in Figure 1[3]. A Gaussian point spread function was applied to reduce the effect of noise in both the spatial and energy dimensions, with a standard deviation of 0.53 eV in the energy dimension and 1 pixel in the spatial dimensions.

The Hyperspy package for python[5] was used to perform the spectral decomposition presented in Figure 4. Three SEHI images of both amorphous and semi-crystalline P3HT samples were analysed together by the same decomposition algorithm, to ensure the generated components were consistent for both samples and across different areas of the same sample. Pixel binning with a factor of 3 was used for this analysis (i.e., 3x3 pixel areas were analysed as single pixels) to reduce the impact of shot noise on the analysis. Further, the integrated SE intensity of each analysed SEHI image was normalised across the full measured SE energy range prior to decomposition. Spectral decomposition was performed with a non-negative matrix factorisation (NMF) algorithm, in order to ensure all factors and loadings generated by the algorithm were physical (i.e. ≥ 0). We found that the first two components output by this algorithm excellently described the spectral variance found in the localised SE spectra of P3HT samples.

nano-FTIR

For mid-IR near-field spectroscopy, a commercial scattering-type scanning near-field optical microscope was used (neaspec GmbH, Germany). The system is based on standard AFM technology where a conventional metal-coated (Pt/Ir) tip is oscillating in intermittent contact vertically to the sample surface. The tip acts simultaneously as an AFM probe and as a near-field probe[6]. Tip and sample are illuminated via a parabolic mirror objective with a broadband mid-infrared supercontinuum laser (neaspec GmbH, max. frequency range ca. 650–2200 cm^{-1} , with average 1 mW power), which is generated by difference frequency generation. The tip-scattered light is analyzed with an asymmetric Fourier transform spectrometer where tip and sample are located in one of the interferometer arms. The detector signal is demodulated at a frequency $2f$ ($2\times$ AFM tip oscillation frequency) for effective background suppression. An interferogram is measured by recording the demodulated detector signal as a function of the position of the reference mirror at a fixed tip position. Subsequent Fourier transform of the recorded interferogram yields the complex-valued near-field point spectrum from the 10nm length scale volume just underneath the AFM-tip. The complex spectrum can be represented as nano-FTIR reflectivity and absorption spectra[7], [8].

Monte Carlo Modelling

A Monte Carlo method was used to simulate the shape of the secondary electron emission peak by considering a monoenergetic electron beam impinging on the investigated material. The trajectories of both primary and secondary electrons were calculated. The electrons escaping from the material were counted as a function of their kinetic energy to obtain the emission spectrum.

In particular the simulation modelled: (i) the elastic scattering between electrons and atomic nuclei, (ii) the inelastic scattering between travelling electrons and target electrons, (iii) the electron-phonon interaction and (iv) the trapping phenomenon[9]. The parameters employed are the properties of P3HT taken from literature[10] ($C_{\text{trap}} = 0.001 \text{ \AA}^{-1}$, $\gamma_{\text{trap}} = 0.105 \text{ eV}^{-1}$). The electron-phonon interaction, which influences the low energy electron region, was treated by applying the Froehlich theory [11]. The value of high frequency and static dielectric constants, respectively equal to $\epsilon_{\infty} = 3.6$ and $\epsilon_0 = 3.0$ [12], were employed in the calculation. Moreover, the single energy loss due to the electron-phonon interaction was set to $W_{\text{ph}} = 0.05 \text{ eV}$.

The inelastic scattering, due to electron-electron cloud interaction, was considered by implementing the Ritchie dielectric theory[13]. It involves the energy loss function, described as a sum of Drude-Lorentz functions representing electron oscillations[14]. The values of the strength, energy and width of the oscillators are those reported in Ref. [15].

The elastic scattering was evaluated starting from the elastic scattering cross section by applying the Mott theory[16]. The P3HT elastic scattering cross section was obtained by a linear combination of elastic cross sections of the single elements composing the molecule. The coefficients of the combination are given by the stoichiometry of the compound. The analytical formulation of atomic potentials by Salvat was used [17]. Moreover, the Ganachaud and Mokrani correction was applied to the total elastic scattering cross section[18] by using the parameter α equal to 0.01.

Secondary electrons are generated as a result of inelastic interactions: if the energy loss of the travelling electron is larger than the threshold energy, this energy is transferred to an electron of a target atom. Thus, the secondary electron is emitted and its trajectory is calculated in the model. The threshold energy, in this case, was set equal to 2.5 eV, a value corresponding to the mean value of energy band gaps found in the literature[19].

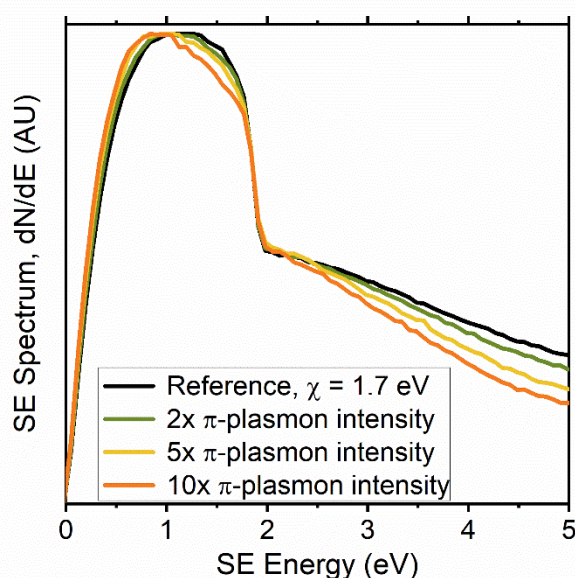
A key role in the calculation is represented by the electron affinity, acting as the energy barrier that electrons must overcome to be emitted. The surface of the P3HT shows amorphous and crystalline regions. To model this feature, regions with different electrons affinities were considered in the simulation.

The modelled SE spectra were compared to the experimental results acquired in the FEI Sirion SEM. The lower dose used to acquire SE spectra in the Sirion SEM means that the spectra in Figure 1a are less likely to be affected by electron beam damage or charging, effects which are not accounted for in the Monte Carlo model.

2. Modelling SE spectra: effect of plasmon energy

In Supplementary Figure 1, we explore the importance of a different modelling parameter, the intensity of π -electron plasmon oscillator, to the shape of the modelled SE spectrum (Figure 4, main work). This is a useful sample feature in the discussion of molecular ordering, as the strength of the π -plasmon has been closely related to the presence of molecular ordering in the material in electron energy loss spectrum (EELS) studies in the TEM[20], [21]. Considering SE spectroscopy, the excitation of π plasmons is a significant source of energy loss for SEs within the material[15], influencing the shape of the SE spectrum as a result[15], [22].

Our previous work[15] showed that the average π -plasmon oscillator is ~ 1.5 times stronger in P3HT films having a higher degree of crystallinity (localised differences may be considerably larger, however). The results in Supplementary Figure 1 show that suggest that crystalline P3HT phases with a (considerably) stronger π -electron structure would display a spectrum peak at lower energies. We expect this trend from our experimental studies in Figure 1. Supplementary Figure 1 suggests this effect is relatively small in comparison to that of electron affinity (Figures 3b-c), and as such we expect that electron affinity remains the dominant effect resulting in the strength of peak 1 in Figure 1f.



Supplementary Figure 1: *Effect of π -plasmon intensity on the shape of the simulated P3HT SE spectrum with $\chi=1.7$ eV*

3. References

- [1] P. Kazemian, S. a. M. Mentink, C. Rodenburg, and C. J. Humphreys, “High resolution quantitative two-dimensional dopant mapping using energy-filtered secondary electron imaging,” *J. Appl. Phys.*, vol. 100, no. 5, p. 54901, 2006.
- [2] M. a E. Jepson, B. J. Inkson, R. Beanland, a K. W. Chee, C. J. Humphreys, and C. Rodenburg, “Progress towards site-specific dopant profiling in the scanning electron microscope,” *J. Phys. Conf. Ser.*, vol. 209, p. 12068, Feb. 2010.
- [3] R. C. Masters, A. J. Pearson, T. S. Glen, F.-C. Sasam, L. Li, M. Dapor, A. M. Donald, D. G. Lidzey, and C. Rodenburg, “Sub-nanometre resolution imaging of polymer–fullerene photovoltaic blends using energy-filtered scanning electron microscopy,” *Nat. Commun.*, vol. 6, p. 6928, 2015.
- [4] N. Stehling, R. Masters, Y. Zhou, R. O’Connell, C. Holland, H. Zhang, and C. Rodenburg, “New perspectives on nano-engineering by secondary electron spectroscopy in the helium ion and scanning electron microscope,” *MRS Commun.*, vol. 8, no. 2, pp. 226–240, Jun. 2018.
- [5] F. de la Peña, T. Ostasevicius, V. T. Fauske, P. Burdet, E. Prestat, P. Jokubauskas, M. Nord, M. Sarahan, K. E. MacArthur, D. N. Johnstone, J. Taillon, J. Caron, V. Migunov, T. Furnival, A. Eljarrat, S. Mazzucco, T. Aarholt, M. Walls, T. Slater, F. Winkler, B. Martinea, G. Donval, R. McLeod, E. R. Hoglund, I. Alxneit, I. Hjorth, T. Henninen, L. F. Zagonel, A. Garmannslund, and 5ht2, “Hyperspy 1.3.2.” Zenodo, 2018.
- [6] F. Keilmann and R. Hillenbrand, “Near-field microscopy by elastic light scattering from a tip,” *Philos. Trans. R. Soc. A Math. Phys. Eng. Sci.*, vol. 362, no. 1817, pp. 787–805, Apr. 2004.
- [7] F. Huth, A. Govyadinov, S. Amarie, W. Nuansing, F. Keilmann, and R. Hillenbrand, “Nano-FTIR Absorption Spectroscopy of Molecular Fingerprints at 20 nm Spatial Resolution,” *Nano Lett.*, vol. 12, no. 8, pp. 3973–3978, Aug. 2012.
- [8] I. Amenabar, S. Poly, M. Goikoetxea, W. Nuansing, P. Lasch, and R. Hillenbrand, “Hyperspectral infrared nanoimaging of organic samples based on Fourier transform infrared nanospectroscopy,” *Nat. Commun.*, vol. 8, 2017.
- [9] J. P. Ganachaud and A. Mokrani, “Theoretical study of the secondary electron emission of insulating targets,” *Surf. Sci.*, vol. 334, pp. 329–341, 1995.
- [10] J. Schafferhans, A. Baumann, A. Wagenpfahl, C. Deibel, and V. Dyakonov, “Oxygen doping of P3HT:PCBM blends: Influence on trap states, charge carrier mobility and solar cell performance,” *Org. Electron.*, vol. 11, no. 10, pp. 1693–1700, 2010.
- [11] H. Fröhlich, “Electrons in lattice fields,” *Adv. Phys.*, vol. 3, pp. 325–361, 1954.
- [12] R. Singh, R. K. Singh, J. Kumar, R. Kant, and V. Kumar, “The origin of DC electrical conduction and dielectric relaxation in pristine and doped poly(3-hexylthiophene) films,” *J. Polym. Sci. Part B Polym. Phys.*, vol. 48, no. 10, pp. 1047–1053, May 2010.
- [13] R. H. Ritchie and A. Howie, “Electron excitation and the optical potential in electron microscopy,” *Philos. Mag.*, vol. 36, no. 2, pp. 463–481, Aug. 1977.
- [14] M. Azzolini, T. Morresi, G. Garberoglio, L. Calliari, N. M. Pugno, S. Taioli, and M. Dapor, “Monte Carlo simulations of measured electron energy-loss spectra of diamond and graphite: Role of dielectric-response models,” *Carbon N. Y.*, vol. 118, pp. 299–309, 2017.
- [15] M. Dapor, R. C. Masters, I. Ross, D. G. Lidzey, A. J. Pearson, I. Abril, R. Garcia-Molina, J. Sharp, M. Unčovský, T. Vystavel, F. Mika, and C. Rodenburg, ““Secondary electron spectra of semi-crystalline polymers – A novel polymer characterisation tool?”” *J. Electron Spectros. Relat. Phenomena*, vol. 222, pp. 1–11, Jan. 2017.

- [16] N. F. Mott, "The Scattering of Fast Electrons by Atomic Nuclei," *Proc. R. Soc. A Math. Phys. Eng. Sci.*, vol. 124, no. 794, pp. 425–442, 1929.
- [17] F. Salvat, J. D. Martínez, R. Mayol, and J. Parellada, "Analytical Dirac-Hartree-Fock-Slater screening function for atoms ($Z=1-92$)," *Phys. Rev. A*, vol. 36, no. 2, pp. 467–474, Jul. 1987.
- [18] M. Azzolini, T. Morresi, K. Abrams, R. Masters, N. Stehling, C. Rodenburg, N. M. Pugno, S. Taioli, and M. Dapor, "Anisotropic Approach for Simulating Electron Transport in Layered Materials: Computational and Experimental Study of Highly Oriented Pyrolytic Graphite," *J. Phys. Chem. C*, vol. 122, no. 18, pp. 10159–10166, May 2018.
- [19] K. Kanai, T. Miyazaki, H. Suzuki, M. Inaba, Y. Ouchi, and K. Seki, "Effect of annealing on the electronic structure of poly(3-hexylthiophene) thin film.," *Phys. Chem. Chem. Phys.*, vol. 12, no. 1, pp. 273–282, 2010.
- [20] H. Ahn, D. W. Oblas, and J. E. Whitten, "Electron Irradiation of Poly(3-hexylthiophene) Films," *Macromolecules*, vol. 37, no. 9, pp. 3381–3387, May 2004.
- [21] M. Pfannmöller, H. Flügge, G. Benner, I. Wacker, C. Sommer, M. Hanselmann, S. Schmale, H. Schmidt, F. a Hamprecht, T. Rabe, W. Kowalsky, and R. R. Schröder, "Visualizing a homogeneous blend in bulk heterojunction polymer solar cells by analytical electron microscopy.," *Nano Lett.*, vol. 11, no. 8, pp. 3099–3107, Aug. 2011.
- [22] M. Dapor, *Transport of Energetic Electrons in Solids*. Berlin: Springer, 2014.